ADVANCED ENERGY MATERIALS
www.advenergymat.de

Hierarchically Multiscale Vertically Oriented NiFeCo Nanoflakes for Efficient Electrochemical Oxygen Evolution at High Current Densities

Asim Riaz, Zelio Fusco, Felipe Kremer, Bikesh Gupta, Doudou Zhang, Chennupati Jagadish, Hark Hoe Tan, and Siva Karuturi**

Crucial advancements in versatile catalyst systems capable of achieving high current densities under industrial conditions, bridging the gap between fundamental understanding and practical applications, are pivotal to propel the hydrogen economy forward. In this study, vertically oriented hierarchically multiscale nanoflakes of NiFeCo electrocatalysts are presented, developed by surface modification of a porous substrate with nano-structured nickel. The resulting electrodes achieve remarkably low overpotentials of 139 mV at 10 mAcm^{-2} and 248 mV at 500 mAcm^{-2}. Further, scaled-up electrodes are implemented in a water-splitting electrolyser device exhibiting a stable voltage of 1.82 V to deliver a constant current density of 500 mA cm^{-2} for over 17 days. Moreover, the role of the unique structures on electrochemical activity is systematically investigated by fractal analysis, involving computation of structure factors such as Minkowski connectivity, fractal dimension, and porosity using scanning electron microscope images. It is found that such structures offer higher surface area than typical layered double hydroxide structures due to morphological coherence that results in a superhydrophilic surface, while the base Ni layer boosts the charge transfer. This study demonstrates a Ni/NiFeCo(OH)$_x$ heterostructure with highly porous morphology, a key to unlocking extremely efficient oxygen evolution reaction activity with exceptional stability. Moreover, fractal analysis is presented as a valuable tool to evaluate the electrochemical performance of catalysts for their structured morphology.

1. Introduction

Hydrogen forms a cornerstone of the shift away from fossil fuels to eliminate CO_2 emissions by 2050. Its uptake in energy-intensive economic sectors is deemed essential. Electrochemical water splitting in an alkaline medium is an attractive method for low-cost, industrial-scale hydrogen production with zero process emissions.[1] Research on developing efficient and stable electrocatalysts is vital for a low-cost and durable electrolyser. In particular, due to the sluggish kinetics (high overpotential: $\eta_{anode} > \eta_{cathode}$) and complicated reaction mechanism, oxygen evolution reaction (OER) is considered the rate-limiting step for water splitting reaction.[2] Catalysts such as IrO_2 and RuO_2 have set a benchmark for OER performance, but the high cost and low output current densities of these precious group metals inspire the search for earth-abundant catalysts.

Recently, layered double hydroxide (LDH) structures ($M(OH)_2$, MOOH, where M=Ni, Fe, Co, and Mn) have shown an extraordinary OER activity

A. Riaz, B. Gupta, C. Jagadish, H. H. Tan, S. Karuturi
Department of Electronic Materials Engineering
Research School of Physics
The Australian National University
Canberra, ACT 2601, Australia
E-mail: asim.riaz@anu.edu.au; siva.karuturi@anu.edu.au

The ORCID identification number(s) for the author(s) of this article can be found under https://doi.org/10.1002/aenm.202303001

DOI: 10.1002/aenm.202303001

A. Riaz, Z. Fusco, D. Zhang, S. Karuturi
School of Engineering
The Australian National University
Canberra, ACT 2601, Australia

F. Kremer
Centre for Advanced Microscopy
The Australian National University
Canberra, ACT 2601, Australia

C. Jagadish, H. H. Tan
ARC Centre of Excellence for Transformative Meta-Optical Systems
Research School of Physics
The Australian National University
Canberra, ACT 2601, Australia

comparable to that of precious group metals.[2a,c,3] These architectures hold prominence within the OER electrocatalysts domain due to their distinct morphological attributes, which adeptly unveil the catalytically active sites and amplify the electrochemical surface area.[3a,4] Moreover, their adaptable molecular arrangement enables the fine-tuning of OER behavior through diverse coordination environments and oxidation states brought about by a multitude of transition metal combinations.[2a,5] Corrosion engineering techniques are widely adopted to develop LDH structures because of their facile scalability.[6] For instance, Wen et al.[2b] developed a NiFe-LDH-based OER electrocatalyst using a combination of surface corrosion and electrodeposition techniques, achieving an overpotential of 230 mV to deliver 10 mA cm^{-2} of current density. Similarly, Zhao et al.[6a] synthesized NiFe LDH structures on a corrosion-cell cathode and reported 10 mA cm^{-2} at 188 mV. Nonetheless, the limited adoption of the corrosion engineering technique can be attributed to the sluggish and intricate growth processes involved.

Electrodeposition presents an alternative approach to corrosion engineering, utilizing applied potential to facilitate electron transfer and expedite the formation of uniform films with the desired thickness.[7] More importantly, the one-step electrodeposition method enables room-temperature synthesis of amorphous compounds while affording control over defect incorporation. This has the potential to elevate the OER performance of the electrocatalysts.[6a,8] The electrodeposition technique has been employed to explore diverse electrocatalysts characterized by a spectrum of 2D and 3D morphological configurations. These structures exhibit improved OER performance in comparison to those prepared using an alternative solution or solid-state methodologies.[7b,8c,9]

Notwithstanding the progress in refining structural aspects and identifying optimal transition metal combinations, the kinetics of the OER in these electrocatalysts remains a significant impediment to the practical implementation of commercial-scale electrolyser systems.[3a,8c,10] Research investigations have both empirically and theoretically examined the chemical composition to comprehend and enhance the electrocatalytic efficacy of the catalyst materials.[2b,11] While numerous research articles have documented electrocatalysts exhibiting both porous and nonporous configurations, the understanding of the role that structural morphology plays in influencing electrocatalytic performance remains limited.[3a,12] Furthermore, commonly utilized 3D porous substrates, such as Ni foam, exhibit restrictions that hinder their suitability for integration into commercial zero-gap electrolyser systems. This underscores the need for a methodical exploration of electrocatalyst structures deposited through straightforward and scalable techniques onto electrode substrates compatible with zero-gap electrolyser systems.

In this study, we present an approach to fabricate a remarkably porous and hydrophilic $NiFeCo(OH)_x$ electrocatalyst featuring HM–VON structures for highly efficient OER activity. The effect of surface modification toward achieving such structures is highlighted in terms of conductivity and charge transfer between the catalyst–Ni interface. Furthermore, factors affecting the growth of these porous structures such as stoichiometric ratios of Ni, Fe, and cobalt, substrate, and parameters of the electrodeposition technique are explored. Where, the role of cobalt addition on the size of nanoflakes and growth of flower-like structures on Ni-modified substrate are presented. Enhanced OER activity of the catalyst electrodes is related to the hydrophilicity, achieved on highly porous nanoflake architecture. A thorough examination of these structures is conducted utilizing fractal analysis techniques, enabling the determination of the achieved 2D porosity on various substrates and under different deposition parameters. An important aspect explored in this study is "Minkowski connectivity," which highlights the significance of lateral connectivity among flakes within 2D porous structures toward charge transfer for electrochemical reactions. In summary, this study emphasizes a methodical evaluation of electrocatalyst structure for water splitting performance and orients the research efforts toward use in industry for low-cost and efficient hydrogen production.

2. Results and Discussion

2.1. Morphological Optimization

Different compositions of Ni, Fe, and Co elements with various stoichiometric ratios were deposited onto the nickel foam to determine the most efficient and stable OER performance. Clearly, an equimolar mixture of Ni, Fe, and Co showed promising OER results as compared to NiFe and NiCo, as shown in Figure S2 (Supporting Information).

Further, the Electrodeposition process was optimized to achieve the HM–VON structures onto substrates suitable for commercial electrolyser systems. Surface morphologies of the as-synthesized NiFeCo electrocatalyst on NF, PNF, SSF, and Ni/SSF were characterized by SEM. The choice of substrate was made by considering the electrochemical characteristics and suitability to be used in a zero-gap configuration.

An alternative to NF, SSF was evaluated as a potential substrate candidate for catalyst deposition. SSF has been widely utilized in commercial electrolysers as a gas diffusion layer sandwiching catalyst-coated anion exchange membrane. Coating porous electrocatalysts directly onto the gas diffusion layer could significantly reduce interfacial resistance while avoiding any bubble build-up between the thick catalyst and gas diffusion layer. Here, smaller diameter wires in SSF provide a higher degree of micro-porosity leading to enhanced surface features of the catalyst which could be helpful to increase the OER performance. This can be confirmed in the surface morphological analysis of NiFeCo electrocatalyst with similar a VON structure but smaller nanoflakes as compared to the one deposited on NF (Figure S5, Supporting Information).

The surface of the SSF substrate was modified by electroplating Ni prior to the coating of NiFeCo electrocatalyst. The nanostructured Ni surface promoted a homogeneous growth of the HM–VON structures as compared to the bare SSF substrate, as confirmed by the SEM image of the as-deposited NiFeCo–Ni–SSF electrode in **Figure 1**a. In addition, the density of these flower-like structures of NiFeCo increased on Ni–SSF substrate, resulting in multiscale porous vertically oriented nanostructures as shown in Figure 1b,c. A thin layer of Ni is also advantageous in terms of improving the surface conductivity of the SSF which is higher than nickel foam itself. Where, high current densities for Ni–SSF sample (Figures S7 and S8, Supporting Information) depict lower ohmic resistance and efficient charge transfer than NF, which

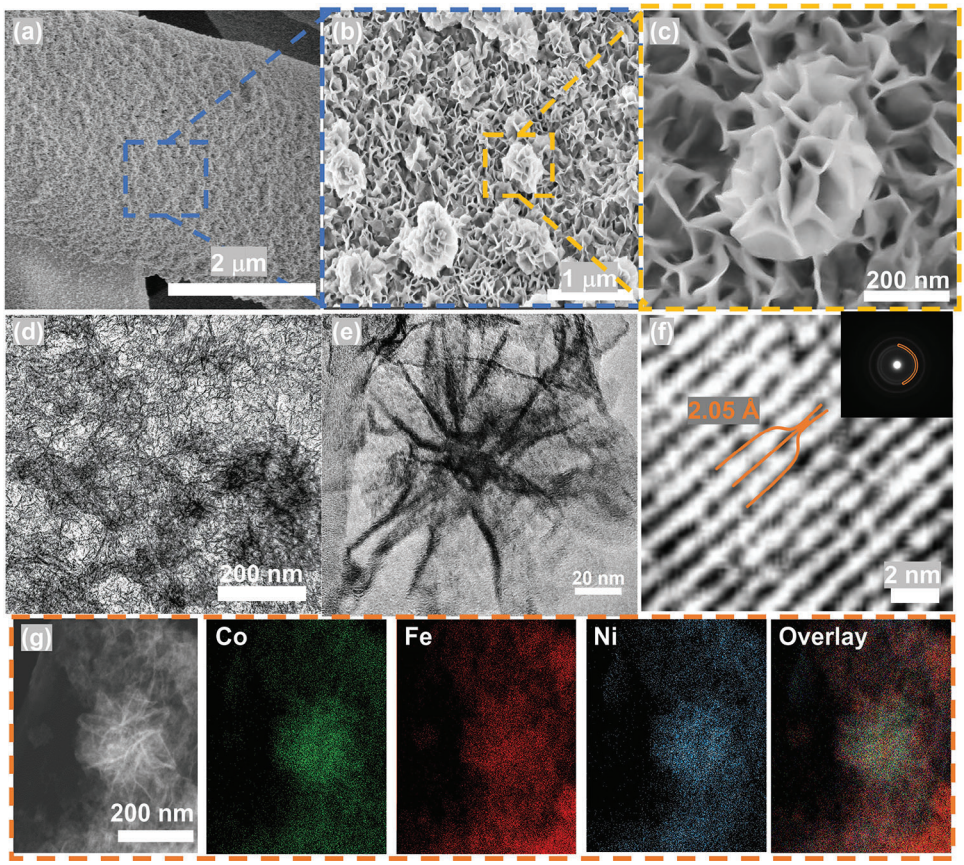

Figure 1. Structural and compositional analysis of NiFeCo HM–VON structures: a–c) SEM micrographs of as-deposited NiFeCo catalyst on Ni–SSF substrate at different magnifications, showing homogeneously dispersed flower-like structure onto the porous nanoscale network. d) TEM image of as-prepared NiFeCo electrocatalyst with dark and light regions, showing NiFeCo making a porous network, e) shows the flower-like structure made up of NiFeCo nanoflakes. f) HRTEM image of a NiFeCo nanosheet and insert shows amorphous rings in SAED image. g) STEM–EDS elemental mapping of the LDH nanoflakes showing the distribution of Co, Fe and Ni elements.

significantly contributes toward the intended use of the NiFeCo HM–VON catalyst electrodes for electrolyser devices requiring high current densities.

Transmission electron microscopy (TEM) image in Figure 1d,e represents the wrinkled NiFeCo sheets with vertically oriented morphologies. The high-resolution TEM image (Figure 1f) of the nanosheet exhibits lattice fringes of NiFeCo with a spacing of 2.05 Å, and insert contains the SAED image, showing amorphous rings of the NiFeCo(OH)$_x$ phase. Elemental mapping in the STEM–EDS analysis in Figure 1g shows a uniform distribution of Ni, Fe, and Co on the substrates.

2.2. Compositional Characterization

X-ray diffraction analysis of the as-deposited NiFeCo deposited onto the Ni–SSF substrate shows distinct diffraction peaks of NiFeCo LDH structure (ICSD # 96-900-0089) mainly with (012), (015), (110), and (113) plane, which reflects of an amorphous hydrotalcite-like structure of VON nanosheets. While LDH nature of NiFeCo is evident from the signature peaks ((003), (006), and (002)), as shown in **Figure 2**a.[14] Raman spectrum of as-prepared NiFeCo–Ni–SSF, NiFe–Ni–SSF, and Ni–SSF samples shows a band at ≈550 cm^{-1} which is associated with the one-phonon (1P), while two-phonon vibrational modes of NiO can be observed at ≈700 cm^{-1} (Figure 2b). A downward shift of ≈25 cm^{-1} in the wavenumber is noted for the 2P vibrational mode in the NiFeCo–Ni–SSF sample. This phenomenon can be ascribed to the elongation of the Ni—O bond due to the incorporation of Co into NiFe. This interpretation gains further support from the discernible peak at 525 cm^{-1} corresponding to the Ni—O bond in the spectrum. The presence of Co—O is observed due to a peak of *Eg* vibrational mode at 480 cm^{-1}.[15]

The as-prepared materials underwent additional characterization using XPS, aimed at assessing both the electronic structure and surface properties of the NiFeCo(OH)$_x$ electrocatalyst, which was deposited onto the Ni–SSF substrate. Wide-range scanning of the XPS spectrum revealed the co-existence of Ni, Fe, Co, and O elements after deposition, while no obvious signals of Fe and Co are observed in the XPS spectrum of the Ni–SSF electrode. The Ni 2P$_{3/2}$ peak at 855.5 eV in the Ni 2P spectrum shows Ni—O species, as shown in Figure 2c. Nevertheless, the multiplet splitting of the Ni 2P$_{3/2}$ peak observed on the surface of the Ni–SSF electrode indicates a transformation from surface NiO species to predominantly M—OH species following the deposition of NiFe

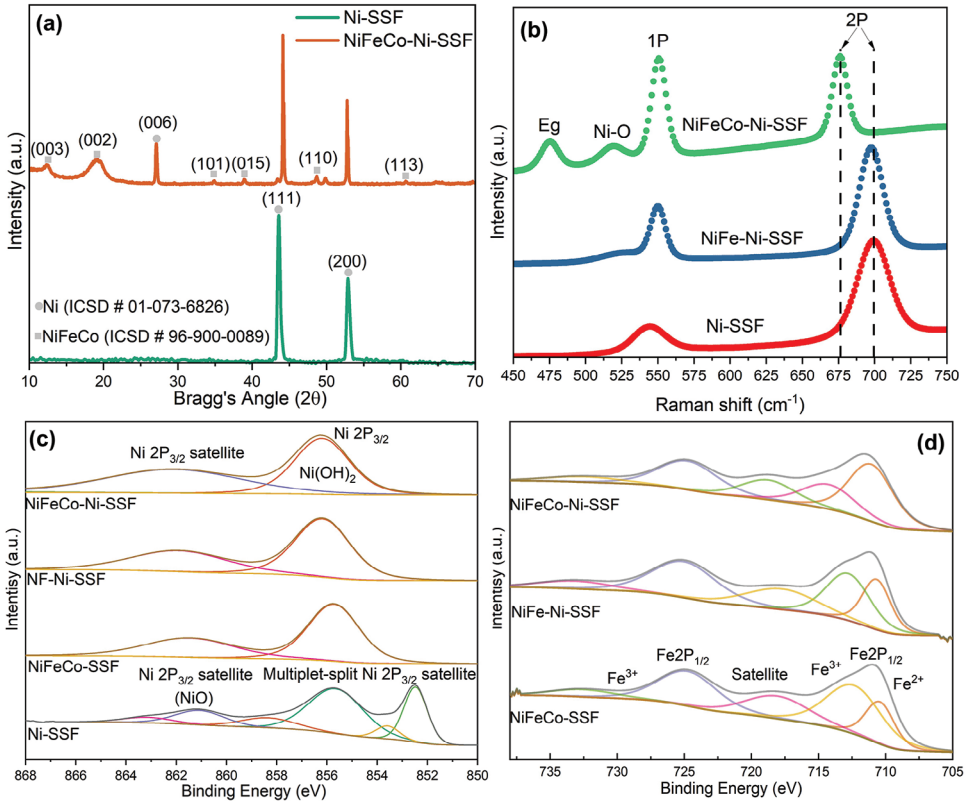

Figure 2. Structural characterization of NiFeCo electrocatalyst: a) X-ray diffraction pattern of Ni-SSF and NiFeCo-Ni-SSF electrodes. b) Raman spectra of as prepared Ni-SSF, NiFe–Ni–SSF and NiFeCo–Ni–SSF electrodes showing distinct characteristics of metal-oxides and hydroxide vibrational bands. High-resolution XPS spectra of c) Ni 2P and d) Fe 2P, depicting the oxidation states and electronic structures of Ni, and Fe elements, respectively.

and NiFeCo. This is substantiated by the presence of a singular Ni $2P_{3/2}$ peak.[2b] In Figure 2d, the Fe 2P spectrum is meticulously fitted with a pair of discernible peaks: the Fe $2P_{3/2}$ peak at 710.2 eV and the Fe $2P_{1/2}$ peak at 722.4 eV. This spectral pattern unequivocally corresponds to the +2 oxidation state of iron (Fe).[2b] The meticulous deconvolution of these peaks, namely the $2P_{3/2}$ peak at 713.2 eV and the Fe $2P_{1/2}$ peak at 724.9 eV, distinctly uncovers the presence of surface-bound Fe^{3+} species. Conversely, a prevalence of Fe^{2+} species at 710.5 eV is noted in the NiFeCo–Ni–SSF sample, contrasting with the NiFe-Ni-SSF and NiFeCo-SSF samples. XPS spectra of Co with $2P_{3/2}$ peaks at 781.6 eV and Co $2P_{1/2}$ at 796.7 eV can be attributed to the +3 oxidation state of cobalt (Figure S10, Supporting Information). The O 1s core level spectrum depicts two distinct peaks i.e., M—O and M—OH for both NiFeCo–SSF and NiFeCo–Ni–SSF electrodes unveiling the coexistence of mixed oxides and the hydroxide characteristics (Figure S11, Supporting Information). No obvious difference in positioning of the M—O peaks is observed for both the electrode surfaces which are located at 529.2 eV. However, a larger M—O peak area depicts higher concentrations of Ni—O species on the NiFeCo–SSF electrode than on the NiFeCo–Ni–SSF surface. In addition, a peak attributed to the lattice oxygen in the O 1s spectrum is shifted to higher binding energy, which indicates layered double hydroxide structure (—Ni (Fe)—O—Fe—Co) as the dominating species in NiFeCo–Ni–SSF as compared to NiFeCo–SSF.[2b] These strongly coupled interfaces in the LDH heterostructures significantly influence the electron injection from Ni to the NiFeCo surfaces, which plays a key role in faster catalytic kinetics.

2.3. Electrochemical Characterization

To evaluate the electrocatalytic OER performance, linear scale voltammetry analysis is performed on the electrodeposited NiFeCo HM–VON structures, along with NiFe LDH, Ni–SSF, and bare NF substrates for reference. 1 M KOH solution was used as the electrolyte, while Pt and SCE were used as counter and reference electrodes, respectively.

After NiFeCo electrocatalyst coating, both the NF and Ni–SSF electrodes exhibited a marked enhancement in their OER activity. This enhancement can be attributed to the activation of a more conductive NiOOH phase, facilitated by the charge transfer effect imparted by the presence of cobalt and iron. Furthermore, the notably low onset potential (1.36 V) observed in the NiFeCo–Ni–SSF configuration can be attributed to the oxidation of Ni^{2+} to Ni^{3+} (**Figure 3**a), a phenomenon brought about by the incorporation of cobalt and iron.[16] The introduction of cobalt led to a noticeable shift of the redox reactions toward lower potentials, as shown in Figure S12 (Supporting Information). This phenomenon is attributed to the enhanced charge transfer occurring within a strained lattice resulting from the inclusion of cobalt, which proves more effective than the underlying NiFe-LDH structure.

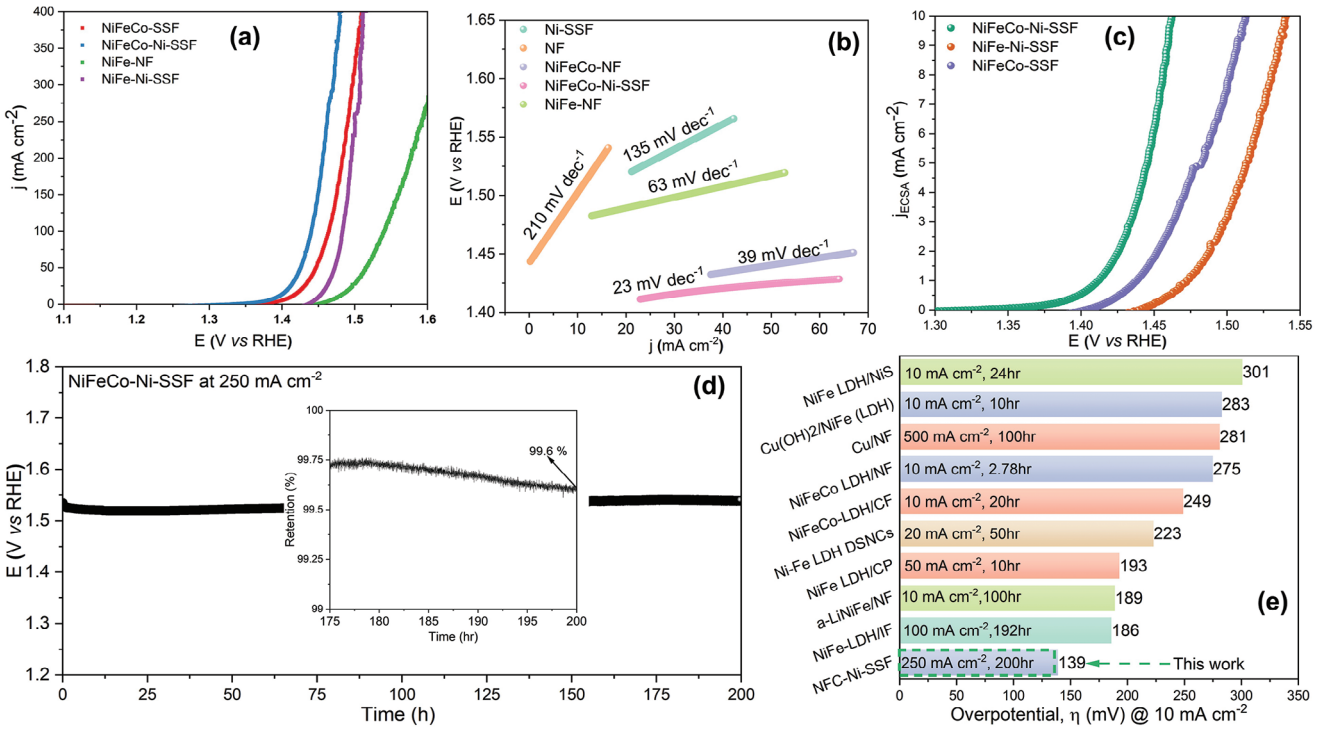

Figure 3. Electrochemical performance evolution: a) Polarization curves, b) Tafel plots c) linear sweep voltammetry (LSV) curves normalized by ECSA of catalyst-coated electrodes showing remarkable OER activity of NiFeCo HM–VON structures on Ni-coated SSF. d) Long-term three-electrode stability of NiFeCo–Ni–SSF electrode at 250 mA cm^{-2}. e) Comparison of the IR-compensated overpotentials at 10 mA cm^{-2} and stability at operational current densities in 1 M KOH solution of various electrocatalysts from the recent literature.[2b,6a,11,17]

Remarkably, the required overpotential to deliver 10 mA cm^{-2} is reduced to 139 mV with NiFeCo HM–VON structures deposited on Ni–SSF substrate as compared to 180 and 230 mV for NiFeCo–SSF and NiFe–Ni–SSF electrodes, respectively. This is reflected by the impedance study of bare and catalyst-coated electrodes, where the trend of resistance follows NiFeCo–Ni–SSF < NiFeCo–SSF < NiFe–Ni–SSF < NiFe–NF < Ni–SSF < NF, as shown in Figure S13 (Supporting Information). Table S1 (Supporting Information) provides a comprehensive summary of the impedance study conducted on both uncoated and catalyst-coated electrodes. Notably, the NiFeCo–Ni–SSF electrode emerges with the most favorable results, exhibiting the lowest resistance values for both solution and circuit resistances. In addition, nanostructured Ni on SSF performs better in terms of OER kinetics, which is reflected in a lower (135 mV dec^{-1}) Tafel slope than bare NF (210 mV dec^{-1}), as shown in Figure 3b. Furthermore, the NiFeCo–Ni–SSF electrode has a Tafel slope of 23 mV dec^{-1}, followed by 39 and 63 mV dec^{-1} for NiFeCo–NF and NiFe LDH–NF electrodes. Nanostructured NiFeCo, featuring a nano-flake morphology on a nickel base, demonstrates advantageous kinetics in facilitating the oxygen evolution reaction. This superiority can be attributed to the increased availability of active sites within the nanoflakes, enhancing the efficiency of the oxygen evolution reaction in contrast to the comparatively less active bulk NF counterpart. Here, it is worth noting the intrinsic OER activity of catalyst electrodes which is obtained by dividing its polarization curve (current densities) by the electrochemically active surface area. As shown in Figure 3c, the intrinsic activity of the NiFeCo–Ni–SSF electrodes is significantly boosted as compared to NiFeCo–SSF and NiFe–Ni–SSF samples.

The long-term stability of the NiFeCo–Ni–SSF electrode is evaluated for OER activity at 250 mA cm^{-2} current densities in a three-electrode measurement setup at room temperature as shown in Figure 3d. Negligible decay in applied potential is observed during the continuous 200 h test while retaining 98.6% of its performance, suggesting its remarkable durability at higher current densities. For comparison, the overpotentials and stability for recently reported OER electrocatalysts are shown in Figure 3e and Table S2 (Supporting Information). The NiFeCo–Ni–SSF electrode outperforms the reported electrodes with the lowest overpotential (139 mV at 10 $mAcm^{-2}$), and superior stability tested for over 200 h at high current densities (250 mA cm^{-2}), when compared to the recently reported work.

Specific intrinsic activities are assessed by normalizing their electrocatalytic activities to the electrochemically active surface area, using the double layer capacitance (C_{dl}) method based on cyclic voltammetry, as shown in Figure S14a (Supporting Information). The high electrochemically active surface area of NiFeCo–Ni–SSF electrode for OER activities is indicated by its higher double-layer capacitance value (9.62 mF cm^{-2}) as compared to the NiFe-LDH structures with a value of 0.775 mF cm^{-2}.[18] In Figure S14b (Supporting Information), it is evident that the NiFeCo–Ni–SSF electrode exhibits a notably larger electrochemically active surface area in comparison to NiFeCo–SSF. This observation indicates that the augmentation in surface area predominantly underlies the enhancement in

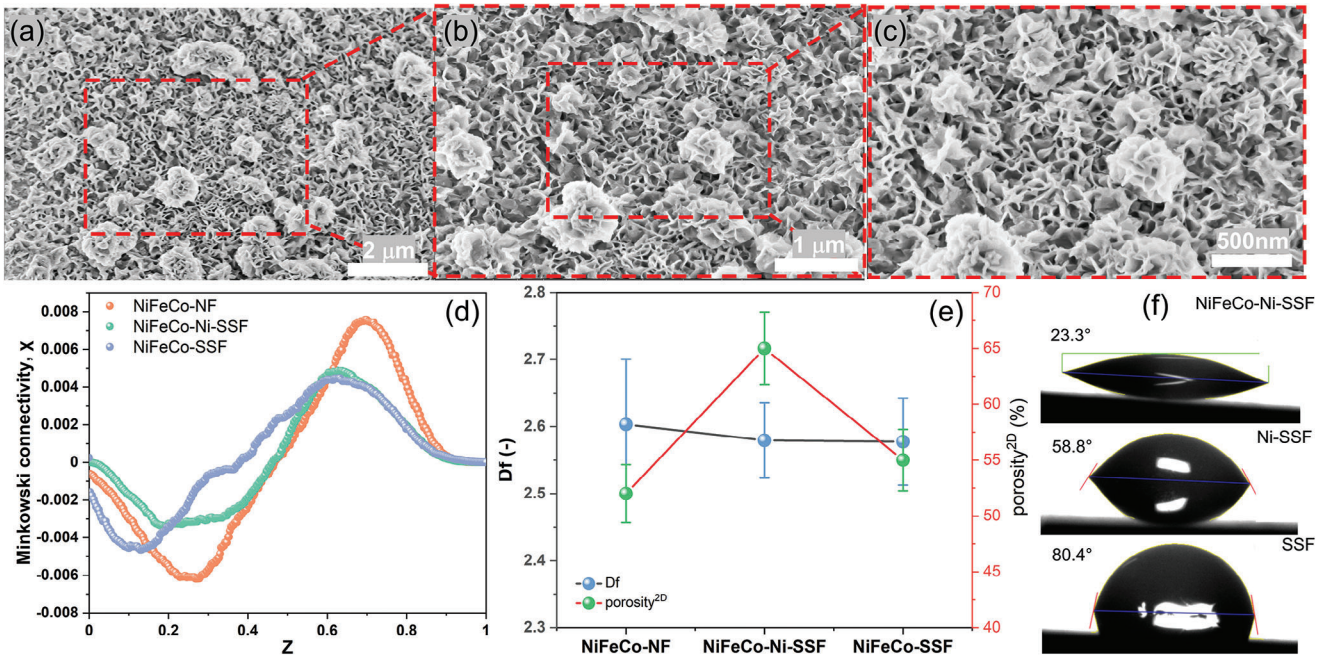

Figure 4. a–c) Scanning electron microscopy images of the NiFeCo–Ni–SSF catalyst showing self-similar properties at different magnifications. d,e) Minkowski connectivity, fractal dimension and porosity, respectively, computed for the NiFeCo–NF, NiFeCo–Ni–SSF and NiFeCo–SSF catalysts. f) Contact angle measurements of Ni-coated, NiFeCo–Ni and NiFe–LDH on bare SSF felt substrate depicting efficient wetting on NiFeCo–Ni–SSF felt electrode.

OER activity. This enhancement can be further attributed to the synergistic effects of cobalt incorporation, which facilitates efficient charge transfer the Ni/NiFeCo and Ni/NiFe interfaces. For instance, NiFe–Ni–SSF possesses higher ECSA than NiFeCo–SSF electrode due to a high population of HM–VON structures, and low ohmic resistance due to efficient charge transfer over the Ni/NiFe interface. However, the NiFeCo electrocatalyst is proven to outperform NiFe, which is evident by lower overpotentials exhibited by NiFeCo–SSF than that of NiFe–Ni–SSF electrodes.

The turnover frequency (TOF) of nickel active sites experiences an impressive nearly threefold increase in the case of NiFeCo–Ni–SSF electrode, as compared to the NiFeCo–SSF configuration. When comparing the respective current densities at an overpotential of 270 mV, the NiFeCo–Ni–SSF electrode exhibited a threefold increase in the TOF values at a remarkable current density (563 mA cm^{-2}) when compared to the NiFeCo–SSF electrode. This is corroborated by the correlation between TOF and overpotential, where the NiFeCo–Ni–SSF electrode emerges as the prominent leader among the various samples, (Figure S14d, Supporting Information). TOF quantification relative to the Fe and Co active sites is carried out by inductively coupled plasma-optical emission spectrometry (ICP–OES). The TOF values based on Ni sites computed from the electrochemical data are close to those acquired from ICP–OES data based on Fe and Co active sites, for the NiFeCo–Ni–SSF samples. However, the Co-TOF and Fe-TOF values are almost half to that of Ni-TOF for the NiFeCo–SSF and NiFe–Ni–SSF electrodes (Figure S19, Supporting Information). Comparing the TOF values depicts the role of each metal active site toward the intrinsic catalytic activity. The role of Ni coating prior to the NiFeCo catalyst deposition should be highlighted for achieving homogeneous elemental distribution that significantly contributes toward remarkable OER performance.

2.4. Fractal Study of the Electrocatalyst

Figure 4a–c shows the characteristic morphology of NiFeCo–Ni–SSF obtained from top-view SEM images taken at magnifications (15×, 35×, and 50×). The catalyst structure possesses a multiscale hierarchical architecture consisting of many porous flower-like clusters deposited onto an interconnected network of self-similar ultrathin VON with widths ranging from 20 to 50 nm. This peculiar morphology could be responsible for the enhanced performance, as such morphology is expected to increase the surface area in contact with the electrolyte and lead to better interfacial charge transport.[3c,19] Conversely, the NiFeCo–NF does not show multiscale features and it is characterized by larger nanosheets with widths ranging from 30 to 90 nm (Figure S20, Supporting Information). On the other hand, the electrodeposition of NiFeCo on SSF leads to nanosheets with the same width of NiFeCo deposited on Ni–SSF but with a sporadic appearance of flower-like structures, as shown in Figure S21, Supporting Information.

Figure 4d plots the Minkowski connectivity for all the catalysts, showing minima in the range of $0 < z < 0.4$ and maxima in the range of $0.5 < z < 0.8$, where z is the normalized greyscale in the SEM images, related to the structure's height.[23] For $z \rightarrow 1$ all structures show a vanishing Minkowski functional, indicating their high connectivity. Particularly, NiFeCo–NF and NiFeCo–SSF are characterized by an equal presence of peaks and valleys, indicated by the same positive and negative magnitudes of the Minkoswki connectivity, |0.007| and |0.004|, respectively. The NiFeCo–Ni–SSF sample shows the least number of valleys/holes (negative peak) indicating that is the most interconnected. This is also confirmed by the analysis of the 2D-porosity computed as the ratio between foreground and background pixels in the SEM images (red line in Figure 4d).[24] NiFeCo–Ni–SSF has a porosity

of 65%, showing an increase of ≈25% and ≈18% compared to NiFeCo–SSF and NiFeCo–NF, respectively. This is attributed to the presence of a multitude of interconnected multiscale flower-like clusters, which increase the porosity and surface area for interaction with the electrolyte.

In summary, this topological analysis demonstrates that despite all the catalysts possessing similar D_f (Figure 4e, black line), they can be distinguished by differences in connectivity and porosity, providing a quantitative approach to assess the relationship between morphology and electrochemical performance. Based on this analysis, we propose that multiple factors contribute to the higher catalytic efficiency of NiFeCo–Ni–SSF: the higher porosity enables larger surface area which facilitates the interaction with the electrolyte while the interconnected networks aided by its crystallinity improve electron transport by reducing electron scattering by grain boundaries.[25]

Surface adsorption of water molecules and electrolyte-catalyst interaction are important determinants for wettability and electrochemical activity of catalysts, respectively. Hence, water contact angles are measured to evaluate the effect of morphology on the wettability of NiFeCo–Ni and NiFe electrocatalyst structures. Figure 4f illustrates much smaller contact angles on NiFeCo–Ni (23.3°) than NiFe-LDH (41°), indicating an enhanced hydrophilic nature of HM–VON structures than a typical LDH structure, which significantly contributes toward efficient OER kinetics.[26] The highly hydrophilic nature of these structures on a porous substrate helps in wetting the catalyst layer. This, in turn, reduces the surface tension that holds the bubble to the surface. As a result, bubbles on hydrophilic surfaces are more likely to detach from the catalyst surface.

This confirms the findings from the fractal analysis, where HM–VON structures demonstrate higher active sites for the OER than the typical LDH structures due to a high degree of interconnectivity and 2D porosity. In addition, the inclusion of the nanostructured Ni layer plays a key role in enhancing the catalytic activity than the bulk NF, which translates into lower overpotentials at the operating current densities.

To better understand the intrinsic phase transformation, Raman spectroscopy analysis was carried out ex-situ and operando. First, the Raman spectra of NiFeCo–Ni–SSF are obtained before and after the OER reaction. A broad band located at ≈530 cm^{-1} is observed in a fresh sample that depicts a distorted LDH structure (Figure S24a, Supporting Information).[15,27–28] After carrying out the OER reaction, the former band disappeared, and two new bands were present at 468 and 550 cm^{-1}, indicating the LDH into NiOOH conversion.[29] Low intensities of these broad bands of NiOOH species reflect complex local environments around Ni—O due to dominant structural defects in the LDH structures caused by the incorporation of Fe and Co, which creates more active sites and enhances the OER activity.[28]

Operando Raman spectroscopy was employed to evaluate alterations in the composition and structure of electrocatalysts during the OER process. A screen-printed electrode (SPE) was used to perform operando Raman spectroscopy on NiFeCo–Ni–SSF electrode. A 0.09 cm^2 sample was placed onto the working electrode (WE) disk region and a droplet of 1 M KOH solution was poured onto the active area of SPE covering WE, counter electrode (CE), and reference electrode (RE), as shown in Figure S24b (Supporting Information). Raman spectra were obtained while performing electrocatalysis reaction in the OER potential ranging from 1.3 to 1.7 V versus RHE, (Figure S24c, Supporting Information). With an increase in potential, the band intensity of $Ni(OH)_2$ located at ≈462 and 525 cm^{-1} showed a decreasing trend. The shifts in Raman bands are usually related to stress/strain generation such as lattice extension contraction, and charge distribution.[30] For instance, stretching of the NiOOH vibrations was observed with a shifting of 475 cm^{-1} toward lower energies, while no obvious change was detected in the m(Ni, Fe, Co)—OOH band at 715 cm^{-1}. Similarly, the band at ≈460 cm^{-1} was slightly blue-shifted due to the Ni^{2+} to Ni^{3+} transition, which caused lattice shrinking by shortening the Ni—O bond.[30a]

Further, chemical alterations on the surface after the OER reaction are assessed by XPS analysis. The Fe2P spectra show an increase in Fe^{3+} species, that depicts Fe^{2+}/Fe^{3+} oxidation (Figure S24d, Supporting Information).[30a] The O 1s region in Figure S25 (Supporting Information) revealed two distinguished peaks OI (529.2 eV) and OII (531.5 eV) representing metal (Ni, Fe, and Co)—O and surface oxygen defect/vacancy, respectively. An increase in the OI peak shows the oxidation of the electrocatalyst after the OER reaction. Moreover, redshift and increased area of OII peak in fresh sample depict a high concentration of surface oxygen vacancies that help enhance the OER activity.[31]

Fractal analysis of catalysts after the OER reaction was carried out to investigate the contribution of porous structures achieved after Ni modification, on the OER activity. From a "nesting" analysis, Ni modification has a significant effect on the OER performance in terms of material stability. The catalysts with Ni and deposited onto SSF retain much of their morphology and a clear nesting (=repetition of morphology at different mags), while the other degrade and undergo a drastic change in morphology/porosity. Figure S24e (Supporting Information) shows the results of the morphological analysis on samples after OER. All samples show a reduction in porosity, however, NiFeCo–Ni–SSF still possesses the highest porosity value. Here it's worth mentioning that retaining the morphological features is also a critical factor to consider along with the 2D porosity, which directly affects the surface area for efficient catalytic activity. This is related to carrying out the Minkowski connectivity analysis on the SEM images (Figures S26–S29, Supporting Information), where a negative ordinate of the Minkowski connectivity plot indicates the presence of many disconnected flat valleys, while a positive one, the presence of disconnected, rough features, Figure S24f (Supporting Information). NiFeCo–Ni–SSF and NiFe–Ni–SSF show the least amount of degradation/dissimilarity between before and after the OER. This is reflected in a similar Minkowski connectivity as before the reaction. NiFeCo–Ni–SSF shows the least number of valleys/holes (negative peak), indicating that it is still the most interconnected. NiFe–Ni has still a good interconnection, indicated by the low negative peak, but also shows a high value of disconnected rough features, due to a large amount of submicron aggregates/structures. NiFe–NF has a sharp negative peak, Indicating the presence of numerous isolated voids.

2.5. Zero-Gap Electrolyser Testing

Electrodes for water splitting in industrial electrolysers generally require current densities over 500 mA cm^{-2}.[2b] Large area up

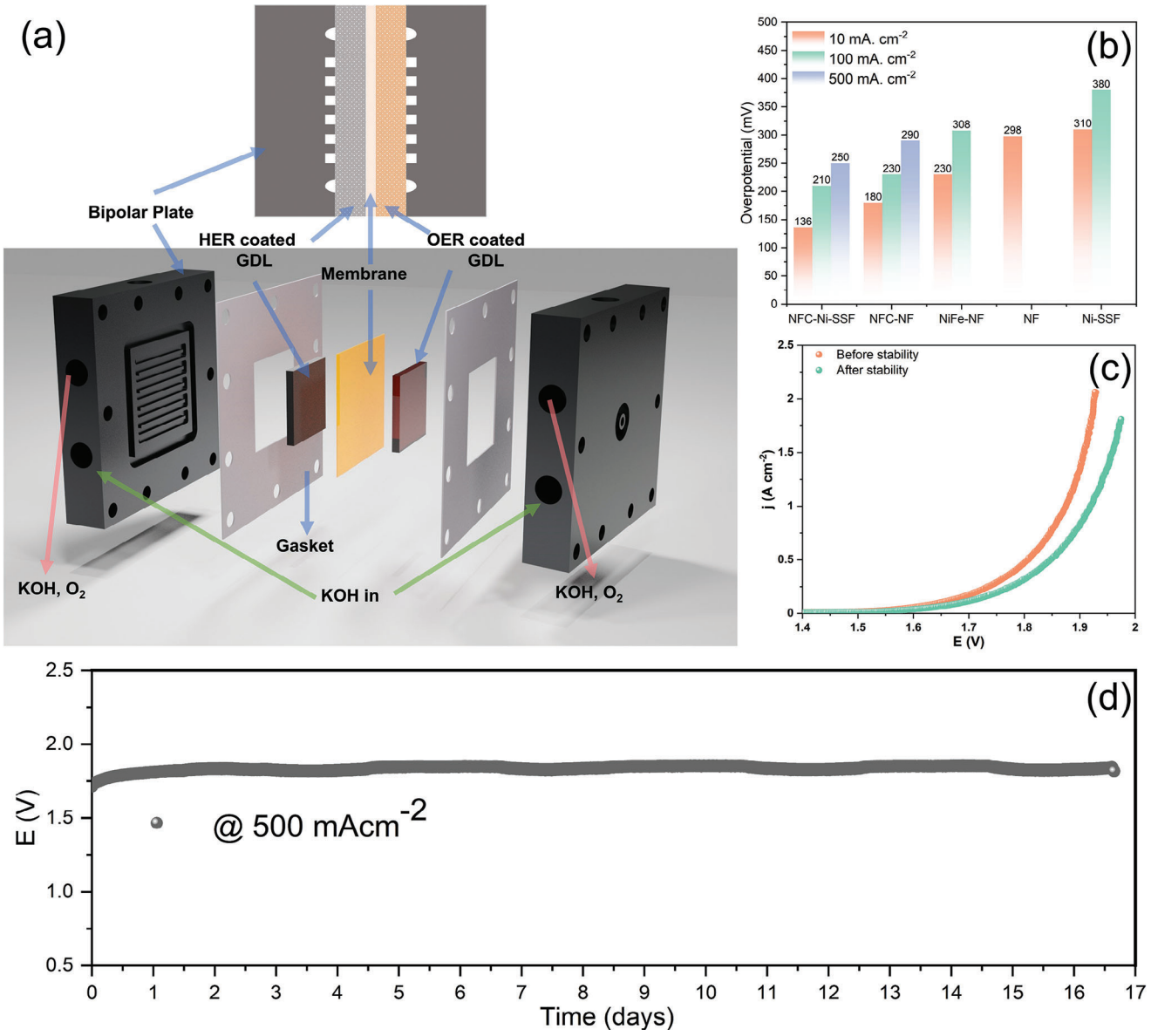

Figure 5. Electrochemical performance of NiFeCo–Ni–SSF electrodes in a zero-gap electrolyser: a) Illustration of a zero-gap device consisting of an OER and HER coated porous electrodes, separated by an anion exchange membrane. b) Overpotentials required to achieve 10, 100, and 500 mA cm^{-2} current densities on various bare and catalyst-coated electrodes. c) Polarization curves of NiFeCo–Ni–SSF || Pt–PNF electrodes in the electrolyser device, before and after stability run at 500 mA cm^{-2}, d) 17 days stability evaluation of NiFeCo–Ni–SSF || Pt–PNF electrodes in the electrolyser device at 500 mA cm^{-2}.

to 12 cm^2 NiFeCo–Ni–SSF electrodes is evaluated for a lab-scale zero-gap alkaline water electrolyser device. **Figure 5**a presents the schematic illustration of the electrolyser device. Both the electrodes (NiFeCo–Ni–SSF for OER and Pt-PNF for HER) are separated by an anionic exchange membrane (Sustanion X37-50 from Dioxide Materials). A thin (10 nm) Pt layer is coated onto the PNF substrate (Pt-PNF) via the e-beam technique, which is used as a cathode. 1 M KOH with a flow rate of 3 mL min^{-1} flow rates was used to perform electrochemical testing at 40 °C. Figure 5b shows a significant reduction in the overpotentials at 10, 100, and 500 mA cm^{-2} for NiFeCo–Ni–SSF electrodes when compared to those of NiFeCo–NF and NiFe–NF electrodes. Despite higher impedance than that of bare NF substrate, Ni coating on SSF electrode plays a key role in achieving high current densities as depicted in Figure 5b.

Linear sweep voltammetry plots are acquired in a potential range of 1.4–2.0 V with a scanning rate of 50 mV s^{-1}, as shown in Figure 5c. The electrolyser system achieved impressive stability at 500 mA cm^{-2} for over 17 days while retaining 97.8% of the starting potential (Figure 5d). The superior catalytic activities and fast OER kinetics of NiFeCo–Ni–SSF electrode requires low cell voltages (1.75 V) to deliver 500 mA cm^{-2}, when coupled with Pt as HER, which significantly surpasses the benchmark Pt–C/IrO_2 pair of electrodes (2.25 V), and further, polarization curves were acquired at RT, 60 and 80 °C.[11] An obvious increase in the current densities above potentials 1.8 V was observed with an

increase in temperature, referring to a reduction in the ohmic resistances, (Figure S30, Supporting Information) Interestingly, an increase in the operating potential is observed in the polarization curve acquired after the stability test (Figure 5d), which may be related to increase in the resistance caused by degradation of membrane. This can be verified by impedance analysis before and after the stability test, where calculated data in fitted the electrochemical impedance spectroscopy curve clearly shows an increase in R_a, R_c, and R_m, as shown in Figure S31 and Table S3 (Supporting Information). The inset in the impedance plot shows the equivalent circuit including the main components. To confirm phase stability of the electrocatalyst, EDS analysis was performed after long-term stability test on the 12 cm^2 electrode. Strong intensities of Ni, Co, and Fe elemental maps depict promising phase stability of the electrodes, Figure S32 (Supporting Information).

Faradaic efficiencies of the NiFeCo–Ni–SSF || Pt–PNF pair of electrodes for the overall water-splitting reaction catalyst are calculated in 1 M KOH to assess the presence of any parasitic reactions. The chromatograms for H_2 and O_2 show a linear increase in the signal intensities with current (Figure S33, Supporting Information). Furthermore, H_2 and O_2 production rates are measured using a gas chromatography technique under continuous water splitting reaction at 40 mA cm^{-2}. The chromatogram at different currents shows a linear increase in O_2 and H_2 species, as indicated in Figure S34 (Supporting Information), which indicates a faradaic efficiency of close to 97% when compared to Ru and NiFe as reference catalysts.

This performance significantly surpasses the recently reported studies on efficient OER electrocatalysts such as NiFe LDH/NiS/commercial Raney Ni achieving only ≈400 mA cm^{-2} at ≈2.1 V in an alkaline water electrolyser using 6.9 M KOH at 80–85 °C.[2b] This demonstrates the suitability of NiFeCo–Ni–SSF OER electrode for alkaline electrolysers without depositing catalysts directly onto the membranes. In this way, the catalyst electrodes can be reused by re-depositing a fresh layer of NiFeCo catalyst on it without the need to replace the costly membrane.

3. Conclusion

In summary, the hierarchically multiscale vertically oriented nanoflakes structure of NiFeCo electrocatalyst was successfully synthesized by surface modification of SSF electrode substrate with Ni. Nanostructured Ni facilitated the formation of nanoflake structures which are deposited homogeneously onto large-area (12 cm^2) electrodes. The as-obtained NiFeCo HM–VON structures exhibited excellent catalytic activity toward the OER, presenting very low overpotentials of 139 and 248 mV at 10 mA cm^{-2} and 500, respectively. The NiFeCo–Ni–SSF electrode demonstrated remarkable stability of over 400 h when tested at constant current densities of 500 mA cm^{-2} (at a low potential of 1.82 V) in a zero-gap water-splitting electrolyser. This shows the suitability of these low-cost earth-abundant catalyst electrodes for large-scale commercial electrolysers. The correlation between topology and electrochemical performance was developed by fractal analysis, which revealed that the 2D porosity and connectivity of such structures greatly influence the electrochemically active surface area. This in turn significantly contributes to achieving high current densities at low overpotentials via efficient local charge and mass transfer at faster rates.

Supporting Information

Supporting Information is available from the Wiley Online Library or from the author.

Acknowledgements

The authors acknowledge the funding support by the Australian Government through the Australian Renewable Energy Agency (ARENA) and the Australian Research Council (ARC). The authors also acknowledge the use of facilities, technical support, and contribution from the ACT Node of the Australian National Fabrication Facility.

Open access publishing facilitated by Australian National University, as part of the Wiley - Australian National University agreement via the Council of Australian University Librarians.

Conflict of Interest

The authors declare no conflict of interest

Data Availability Statement

The data that support the findings of this study are available from the corresponding author upon reasonable request.

Keywords

electrochemical, electrolyze, hydrogen, nanoflakes, oxygen evolution reaction, water splitting

Received: September 7, 2023
Revised: October 11, 2023
Published online: November 15, 2023

[1] J. Song, C. Wei, Z.-F. Huang, C. Liu, L. Zeng, X. Wang, Z. J. Xu, *Chem. Soc. Rev.* **2020**, *49*, 2196.
[2] a) N.-T. Suen, S.-F. Hung, Q. Quan, N. Zhang, Y.-J. Xu, H. M. Chen, *Adv. Energy Mater.* **2021**, *11*, 337; c) J. Zhu, L. Hu, P. Zhao, L. Y. S. Lee, K.-Y. Wong, *Chem. Rev.* **2020**, *120*, 851.
[3] a) P. M. Bodhankar, P. B. Sarawade, G. Singh, A. Vinu, D. S. Dhawale, *J. Mater. Chem. A* **2021**, *9*, 3180; b) E. Nurlaela, T. Shinagawa, M. Qureshi, D. S. Dhawale, K. Takanabe, *ACS Catal.* **2016**, *6*, 1713; c) Y. Wang, D. Yan, S. E. Hankari, Y. Zou, S. Wang, *Adv. Sci.* **2018**, *5*, 1800064; d) L. Lv, Z. Yang, K. Chen, C. Wang, Y. Xiong, *Adv. Energy Mater.* **2019**, *9*, 1803358.
[4] S. Wang, J. Wu, J. Yin, Q. Hu, D. Geng, L.-M Liu, *ChemElectroChem* **2018**, *5*, 1357.
[5] K. Zhang, R. Zou, *Small* **2021**, *17*, 2100129.
[6] a) W. Zhao, H. Xu, H. Luan, N. Chen, P. Gong, K. Yao, Y. Shen, Y. Shao, *Adv. Energy Mater.* **2022**, *12*, 2102372; b) Y. Liu, X. Liang, L. Gu, Y. Zhang, G.-D. Li, X. Zou, J.-S. Chen, *Nat. Commun.* **2018**, *9*, 2609.
[7] a) J. B. Yadav, J.-W. Park, Y.-J. Cho, O.-S. Joo, *Int. J. Hydrogen Energy* **2010**, *35*, 10066; b) R. Li, Y. Li, P. Yang, D. Wang, H. Xu, B. Wang, F. Meng, J. Zhang, M. An, *J. Energy Chem.* **2021**, *57*, 547.
[8] a) O. Mabayoje, Y. Liu, M. Wang, A. Shoola, A. M. Ebrahim, A. I. Frenkel, C. B. Mullins, *J. Mater. Interfaces* **2019**, *11*, 32879; b) X. Cao, D. Jia, D. Li, L. Cui, J. Liu, *J. Energy Chem.* **2018**, *348*, 310; c) M. B. Kale, R. A. Borse, A. Gomaa Abdelkader Mohamed, Y. Wang, *Adv. Funct. Mater.* **2021**, *31*, 2101313.

[9] M. Bernal Lopez, J. Ustarroz, *Curr. Opin. Electrochem.* **2021**, *27*, 100688.
[10] Y. Z. Wang, M. Yang, Y.-M. Ding, N.-W. Li, L. Yu, *Adv. Funct. Mater.* **2022**, *32*, 2108681.
[11] C.-L. Huang, K. Sasaki, D. Senthil Raja, C.-T. Hsieh, Y.-J. Wu, J.-T. Su, C.-C. Cheng, P.-Y Cheng, S.-H. Lin, Y. Choi, S.-Y. Lu, *Adv. Energy Mater.* **2021**, *11*, 2170181.
[12] S. M. Ibn Shamsah, *Catalysts* **2021**, *11*, 429.
[13] G. A. Lindquist, S. Z. Oener, R. Krivina, A. R. Motz, A. Keane, C. Capuano, K. E. Ayers, S. W. Boettcher, *ACS Appl. Materi. Interfaces* **2021**, *13*, 51917.
[14] J. Lee, H. Jung, Y. S. Park, N. Kwon, S. Woo, N. C. S. Selvam, G. S. Han, H. S. Jung, P. J. Yoo, S. M. Choi, J. W. Han, B. Lim, *Appl. Catal., B* **2021**, *294*, 120246.
[15] A. I. Inamdar, H. S. Chavan, S. M. Pawar, H. Kim, H. Im, *Int. J. Energy Res.* **2020**, *44*, 1789.
[16] a) Y. Lin, H. Wang, C.-K. Peng, L. Bu, C.-L. Chiang, K. Tian, Y. Zhao, J. Zhao, Y.-G. Lin, J.-M. Lee, L. Gao, *Small* **2020**, *16*, e2002426; b) M. K. Bates, Q. Jia, H. Doan, W. Liang, S. Mukerjee, *ACS Catal.* **2016**, *6*, 155.
[17] a) X. Ma, X. Li, A. D. Jagadale, X. Hao, A. Abudula, G. Guan, *Int. J. Hydrogen Energy* **2016**, *41*, 14553; b) K. Huang, R. Dong, C. Wang, W. Li, H. Sun, B. Geng, *ACS Sustain. Chem. Eng.* **2019**, *7*, 15073; c) T. Wang, W. Xu, H. Wang, *Electrochem. Acta* **2017**, *257*, 118; d) G. Chen, Y. Zhu, H. M. Chen, Z. Hu, S.-F. Hung, N. Ma, J. Dai, H.-J. Lin, C.-T. Chen, W. Zhou, Z. Shao, *Adv. Mater.* **2019**, *31*, 1900883; e) L. Zhang, X. Huang, H. Dai, M. Wang, H. Cheng, L. Tong, Z. Li, X. Han, X. Wang, L. Ye, J. Han, *Adv. Mater.* **2020**, *32*, 2002032; f) M. Gu, X. Deng, M. Lin, H. Wang, A. Gao, X. Huang, X. Zhang, *Adv. Mater.* **2021**, *11*, 2101937; g) X. Zhu, C. Tang, H.-F. Wang, B.-Q. Li, Q. Zhang, C. Li, C. Yang, F. Wei, *J. Mater. Chem. A* **2016**, 4, 7245; h) M. H. Han, M. W. Pin, J. H. Koh, J. H. Park, J. Kim, B. K. Min, W. H. Lee, H. S. Oh, *J. Mater. Chem. A* **2021**, 9, 27034; i) Y. Lin, H. Wang, C.-K. Peng, L. Bu, C.-L. Chiang, K. Tian, Y. Zhao, J. Zhao, Y.-G. Lin, J.-M. Lee, L. Gao, *Small* **2016**, *6*, 2002426.
[18] Y. Yoon, B. Yan, Y. Surendranath, *J. Am. Chem. Soc.* **2018**, *140*, 2397.
[19] Y. Jia, L. Zhang, G. Gao, H. Chen, B. Wang, J. Zhou, M. T. Soo, M. Hong, X. Yan, G. Qian, J. Zou, A. Du, X. Yao, *Adv. Mater.* **2017**, *29*, 1700017.
[20] I. Levchenko, J. Fang, K. Ostrikov, L. Lorello, M. Keidar, *Graphene* **2016**, *5*, 25.
[21] B. Fazio, P. Artoni, M. Antonia Iatì, C. D'andrea, M. J. Lo Faro, S. Del Sorbo, S. Pirotta, P. Giuseppe Gucciardi, P. Musumeci, C. Salvatore Vasi, R. Saija, M. Galli, F. Priolo, A. Irrera, *Light Sci. Appl.* **2016**, *5*, e16062.
[22] a) Y. Liao, W. Chen, S. Li, W. Jiao, Y. Si, J. Yu, B. Ding, *Small* **2021**, *17*, 2103212. b) P. T. Lillehei, J.-W. Kim, L. J. Gibbons, C. Park, *Nanotechnology* **2009**, *20*, 325708.
[23] M. Pierpaoli, M. Ficek, P. Jakóbczyk, J. Karczewski, R. Bogdanowicz, *Acta Mater.* **2021**, *214*, 116989.
[24] C. Zhao, Y. Qiao, *Nanoscale* **2016**, *8*, 17658.
[25] I. Vladimirov, M. Kühn, T. Geßner, F. May, R. T. Weitz, *Sci. Rep.* **2018**, *8*, 14868.
[26] D. Zhang, H. Li, A. Riaz, A. Sharma, W. Liang, Y. Wang, H. Chen, K. Vora, D. Yan, Z. Su, A. Tricoli, C. Zhao, F. J. Beck, K. Reuter, K. Catchpole, S. Karuturi, *Energy Environ. Sci.* **2021**, *15*, 185.
[27] M. W. Louie, A. T. Bell, *J. Am. Chem. Soc.* **2013**, *33*, 12329.
[28] Z. Lu, A. Xu, A. Zhu, Q. Yang, X. Lei, J. Liu, Y. Li, X. Sun, X. Duan, *ChemComm Commun.* **2014**, *50*, 6479.
[29] J. Desilvestro, D. A. Corrigan, M. J. Weaver, *J. Electrochem. Soc.* **1988**, *135*, 885.
[30] a) Y. Li, M. Yuan, H. Hao, Z. Lv, L. Xu, B. Wei, *Appl. Catal., B* **2022**, 318; b) J. Huang, H. Sheng, R. D. Ross, J. Han, X. Wang, B. Song, S. Jin, *Nature Commun.* **2021**, *12*, 3036; c) Y. Li, Y. Wu, H. Hao, M. Yuan, Z. Lv, L. Xu, B. Wei, *Appl. Catal., B* **2022**, *305*, 121033.
[31] Y. Zheng, K. Fu, Z. Yu, Y. Su, R. Han, Q. Liu, *J. Mater. Chem. A* **2022**, *10*, 14171.